Observation of Exciton Redshift−Blueshift Crossover in Monolayer WS$_2$

E. J. Sie,[†] A. Steinhoff,[‡] C. Gies,[‡] C. H. Lui,[§] Q. Ma,[†] M. Rösner,[‡,∥] G. Schönhoff,[‡,∥] F. Jahnke,[‡] T. O. Wehling,[‡,∥] Y.-H. Lee,[⊥] J. Kong,[#] P. Jarillo-Herrero,[†] and N. Gedik*,[†]

[†]Department of Physics, Massachusetts Institute of Technology, Cambridge, Massachusetts 02139, United States

[‡]Institut für Theoretische Physik, Universität Bremen, P.O. Box 330 440, 28334 Bremen, Germany

[§]Department of Physics and Astronomy, University of California, Riverside, California 92521, United States

[∥]Bremen Center for Computational Materials Science, Universität Bremen, 28334 Bremen, Germany

[⊥]Materials Science and Engineering, National Tsing-Hua University, Hsinchu 30013, Taiwan

[#]Department of Electrical Engineering and Computer Science, Massachusetts Institute of Technology, Cambridge, Massachusetts 02139, United States

S *Supporting Information*

ABSTRACT: We report a rare atom-like interaction between excitons in monolayer WS$_2$, measured using ultrafast absorption spectroscopy. At increasing excitation density, the exciton resonance energy exhibits a pronounced redshift followed by an anomalous blueshift. Using both material-realistic computation and phenomenological modeling, we attribute this observation to plasma effects and an attraction−repulsion crossover of the exciton−exciton interaction that mimics the Lennard-Jones potential between atoms. Our experiment demonstrates a strong analogy between excitons and atoms with respect to interparticle interaction, which holds promise to pursue the predicted liquid and crystalline phases of excitons in two-dimensional materials.
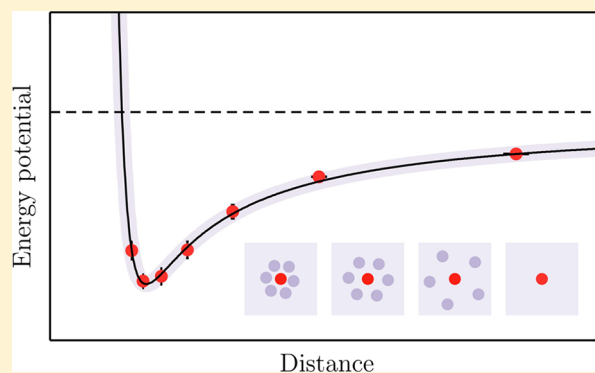
Excitons in semiconductors are often perceived as the solid-state analogues to hydrogen atoms. This analogy helps us to understand the basic features of excitons, notably their internal energy states. However, this analogy breaks down as we consider the interparticle interactions because of some fundamental differences between atoms and excitons. Atoms are stable particles with large ionization energy (∼10 eV). They exhibit long-range van der Waals attraction and short-range Pauli repulsion, which form the so-called Lennard-Jones potential as a function of interatomic separation.[1,2] In contrast, excitons are transient quasiparticles with much smaller binding energy and extremely short lifetime. They can dissociate into an electron−hole plasma, whose relative concentration is governed by the law of mass action.[3,4] Hence, interactions in semiconductors are somewhat different from those in real gases because the effects from plasma[5] and excitons[6] must be considered. The relative importance of exciton and plasma effects depends on the regime of excitation density. In conventional III−V and II−VI semiconductors, such complex many-body effects preclude the demonstration of atom-like interactions between excitons, particularly in the regime of high excitation density where excitons become unstable.

Recent advances in two-dimensional (2D) semiconductors, particularly monolayer transition-metal dichalcogenides (TMDs), offer a unique platform to investigate excitonic interactions. These materials possess strong Coulomb inter-actions due to quantum confinement and reduced dielectric screening,[7] leading to the formation of excitons with exceptionally large binding energies ∼300 meV.[8−11] The enhanced stability of excitons in these materials provides good opportunities to reexamine the role of plasma effects and excitonic interactions over a broad range of excitation density. Although the exciton physics in photoexcited TMDs has been much studied,[12−17] a complete picture of excitonic interactions in these materials is still lacking.

In this Letter, we investigate systematically the many-particle interactions in monolayer WS$_2$. We combine ultrafast absorption spectroscopy, microscopic many-body theory and an analytic approach that maps the measured exciton−exciton interactions onto an effective atomic model. In particular, we measure the absorption spectrum of the A exciton under
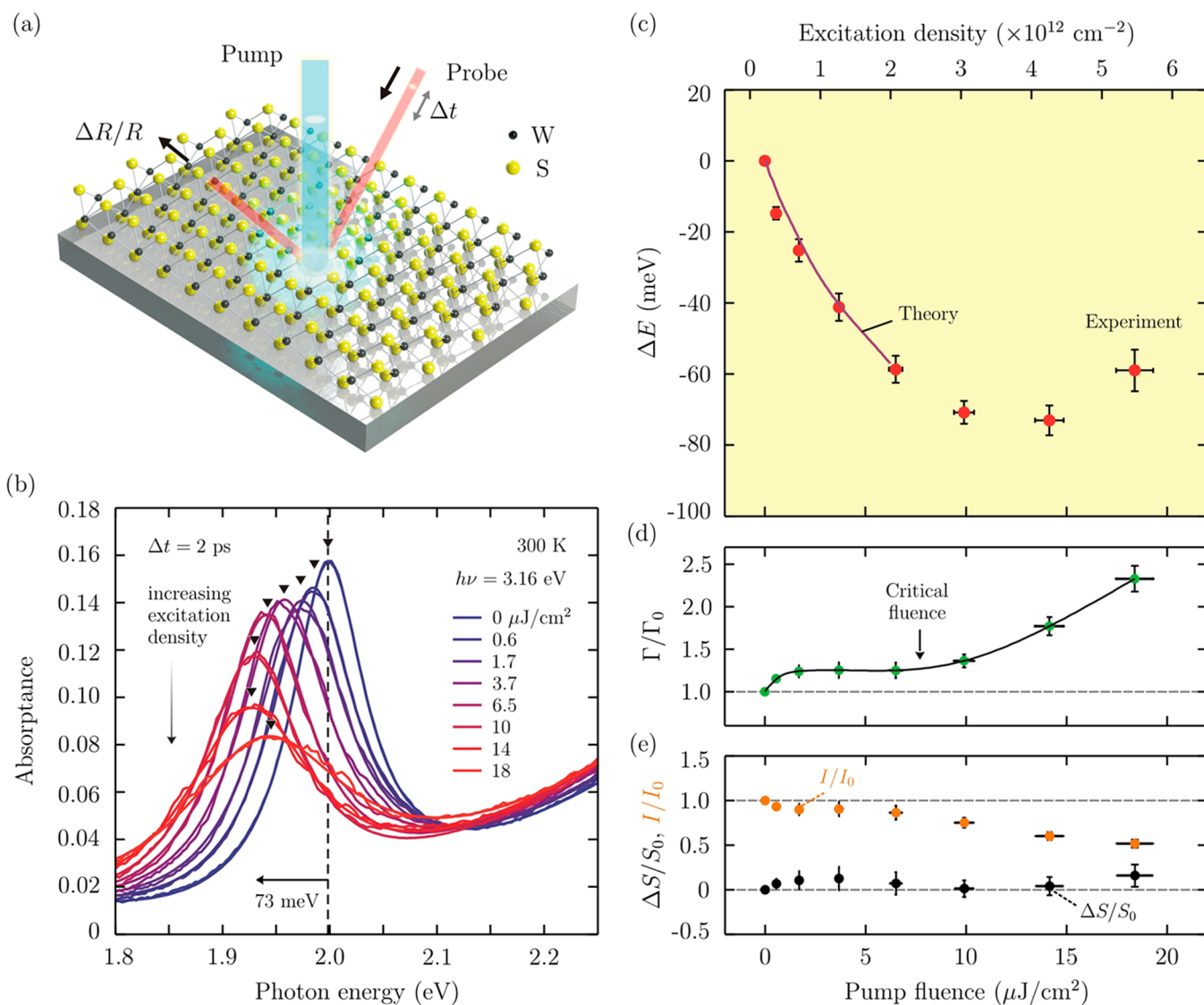
Figure 1. (a) Schematic of transient absorption spectroscopy setup. (b) Absorption peak of A exciton in monolayer WS$_2$ at increasing excitation densities. The fitting lines (smooth lines) are superimposed with the data curves. (c) Exciton energy shift (ΔE) as a function of pump fluence obtained from experiment (red) and calculation (purple). The calculated value terminates at $n = 2 \times 10^{12}$ cm^{-2} due to a Mott transition that is predicted prematurely by the SXCH theory. (d) Line width (Γ/Γ_0), (e) peak height (I/I_0), and spectral weight change ($\Delta S/S_0$).

femtosecond optical excitation. As we increase the excitation density, we observe a pronounced redshift (73 meV) of the exciton resonance energy at low density, followed by an unusual blueshift (10 meV) at high density. We attribute the two different energy shifts to two distinct interaction regimes. At high density, the exciton blueshift is well described by assuming a repulsive exciton–exciton interaction similar to the short-range Lennard-Jones interaction between atoms.[1,2] At low density, the Lennard-Jones potential further contains a long-range contribution due to an attractive exciton–exciton interaction. However, in contrast to the atomic case, the exciton redshift in this regime is found to follow a strongly modified exponent, indicating that not all carriers are bound excitons but a fraction exists as electron–hole plasma. Insight from microscopic theory reveals that the redshift observed at low excitation density mainly arises from plasma-induced bandgap renormalization and screening of the exciton binding energy. We note that the observed energy shift is much larger than those reported in conventional semiconductors such as

GaAs quantum wells (∼0.1 meV)[18–22] as a consequence of the much enhanced many-body interactions in the 2D material. Our model is further supported by the temperature-dependent exciton energy shift observed in the time-resolved absorption measurements.

We investigate monolayer WS$_2$ samples grown on sapphire substrates by chemical vapor deposition.[23–25] In our pump–probe experiment, we generate carriers by femtosecond pump pulses with photon energy of 3.16 eV, well above the quasiparticle bandgap (∼2.3 eV).[11] We then monitor the A exciton resonance near 2.0 eV by recording the reflection spectrum of broadband probe pulses with controlled time delay at room temperature (Figure 1a). For a monolayer sample on a transparent substrate, the absorption spectrum can be extracted from the reflection spectrum using the thin-film approximation (Supporting Information).[14,26] We estimate the excitation density n from the measured incident pump fluence and absorbance of the sample at the excitation wavelength.[26]

Figure 1b shows the absorption spectra of the A exciton at increasing pump fluence up to 18 $\mu J/cm^2$ ($n = 5.3 \times 10^{12}$ cm^{-2}). The spectra were taken at a pump−probe delay of 2 ps, a time after which the excitons are expected to have reached thermal equilibrium with one another and with the lattice but not yet recombined.[27,28] All the spectra can be fitted well with a Lorentzian function plus a second-order polynomial function (smooth lines over the data curves), which represent the exciton peak and the background, respectively (Supporting Information). We note that the B exciton is well separated from the A exciton by 400 meV in monolayer WS_2[26] and therefore does not affect our analysis. From the fitting, we extract the exciton peak energy (E_A), line width (Γ), peak intensity (I), and spectral weight (S, i.e. the integrated area), and plot their changes in Figure 1c−e. While the spectral weight remains unchanged at all excitation densities, the other quantities vary significantly with the density.

These quantities exhibit two distinct behaviors at low and high excitation densities. At low density, the peak energy redshifts gradually for ~70 meV as the density increases, while the line width and peak intensity remain almost constant. The energy shift cannot be explained using the pump-induced lattice heating because the estimated lattice temperature increase is ~20 K, which corresponds to merely ~4 meV of temperature-dependent gap narrowing.[29] In contrast, with further increase of density $n > 2.0 \times 10^{12}$ cm^{-2}, the rate of exciton redshift diminishes and eventually turns into a blueshift of ~10 meV from the lowest energy point. Notably, the redshift−blueshift crossover is accompanied by a large spectral broadening, with the line width increasing to more than twice of the initial width (Figure 1d). Correspondingly, the peak intensity drops to one-half of the initial intensity to maintain the total spectral weight of the A exciton (Figure 1e). These two distinct energy shifts correspond to two different interaction regimes as we will discuss in the following.

We first discuss the redshift at low density. According to prior studies in monolayer TMDs,[5] the exciton redshift can be ascribed to a combination of bandgap renormalization and plasma screening of the exciton binding energy due to the excited unbound carriers (Figure 2a). We have obtained the quasiparticle band structure and Coulomb matrix elements of monolayer WS_2 by first-principle G_0W_0 calculations. Screening from the substrate is additionally incorporated in the Coulomb matrix elements.[30] The exciton shift due to the excited carriers is calculated with microscopic semiconductor Bloch equations in a screened-exchange Coulomb-hole approximation (SXCH); see Supporting Information. With increasing excitation density, both the quasiparticle band gap (E_g) and the exciton binding energy (E_b) are found to decrease (Figure 2b). Since E_g decreases faster than E_b, the resulting exciton resonance energy ($E_A = E_g - E_b$) shifts to lower energies (Figure 2c).

Our calculations reproduce the measured redshift at low density (Figure 1c, purple curve). The overall agreement is remarkable, given that we do not use any fitting parameter in our theory. We note that the SXCH calculation predicts a Mott transition at $n = 2 \times 10^{12}$ cm^{-2}. Approximately at this density, the experimental data reveals a crossover into an anomalous blueshift (Figure 1c), which we attribute to exciton−exciton interaction that is facilitated by the increasing fraction of carriers bound into excitons and marks the limit in carrier density to which a plasma picture applies.

Although the observed redshift at low density is dominated by the plasma contribution, an additional contribution also
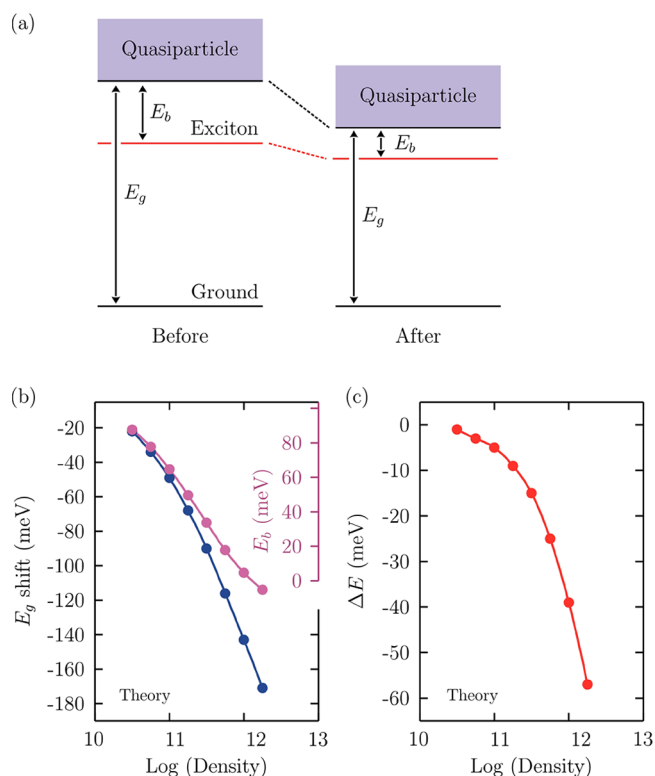

Figure 2. (a) Schematic band diagrams before and after the femtosecond optical pumping. Both the band gap (E_g) and the exciton binding energy (E_b) are reduced after photoexcitation, giving rise to a net downshift of exciton resonance energy. (b) Calculated bandgap narrowing (ΔE_g) and exciton binding energy (E_b) as a function of exciton density in a semilogarithmic scale. (c) The resultant shift of exciton resonance energy (ΔE) at increasing exciton density, as also shown in Figure 1c.

results from exciton−exciton attraction as in the case of atomic van der Waals forces. Mutual attraction can reduce the energy cost to create an extra exciton (E_A) by a magnitude as much as the negative interexciton potential energy. In light of this picture, we interpret the blueshift at high density >8 $\mu J/cm^2$ ($n > 2.0 \times 10^{12}$ cm^{-2}), where a large fraction of carriers form bound excitons, as arising from an exciton−exciton *repulsion*. Indeed, the blueshift is not captured by our numerical approach and therefore suggests a new contribution other than the plasma effects. The simultaneous broadening of the absorption peak indicates that this new interaction strongly perturbs the excitons and shortens their lifetime (Figure 1d). In this scenario, high-density excitons tend to repel each other due to the Pauli exclusion of overlapping electron orbitals, giving rise to positive interexciton potential energy. As a consequence, the energy cost to create an extra exciton increases, leading to a blueshift of the resonance energy.

The above interpretation has inspired us to quantify the excitonic contributions to the energy shift in the entire density range through a simple phenomenological model with two power laws in analogy to the well-known Lennard-Jones potential between atoms (for which $k = 6$):

$$\Delta E = \varepsilon \left[\left(\frac{r_0}{r_s} \right)^8 - \left(\frac{r_0}{r_s} \right)^k \right]$$

(1)

Here r_s is the radius of disk occupied by an exciton ($n\pi r_s^2 = 1$). ε, r_0, and k are the fitting parameters, which can be interpreted in a similar way as in the usual "12−6" power-law potential between atoms. The first term describes the exciton blueshift caused by the short-range Pauli repulsion. We use the r_s^{-8} functional form for better fitting of the Pauli repulsion in this system instead of the usual r_s^{-12} typically chosen in atomic system for convenience due to the relative computing efficiency (r_s^{-12} is the square of r_s^{-6}). The second term models the exciton redshift caused by the long-range van der Waals attraction of excitons behaving as fluctuating dipoles in the presence of plasma in this material. In general, the functional form of this attraction potential can differ from the usual London dispersion force r_s^{-6}; hence, we parametrize it as r_s^{-k}. By fitting the $\Delta E - r_s$ data through the least-squares method with $\varepsilon = 128 \pm 10$ meV, $r_0 = 2.6 \pm 0.1$ nm, and $k = 1.4 \pm 0.2$, our simple model matches precisely the density dependence of exciton energy shift (Figure 3a). Note that we have considered
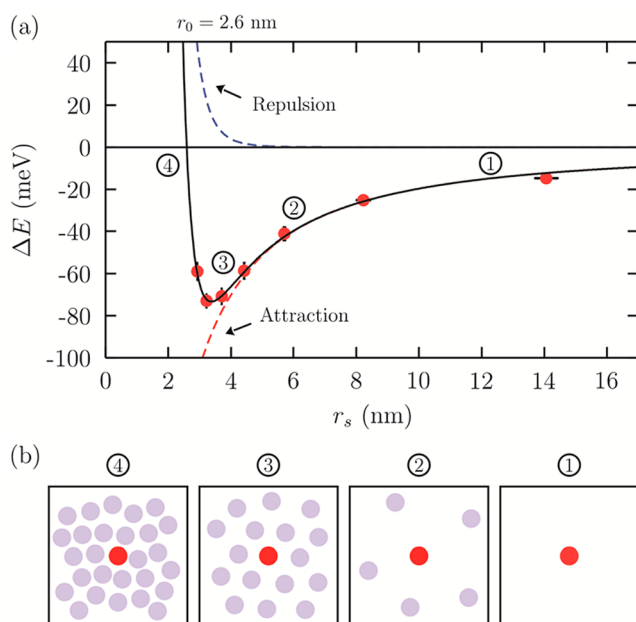

Figure 3. (a) Exciton energy shift (ΔE) as a function of average radius (r_s) occupied by an exciton in the exciton gas. The red dots are experimental data from Figure 1c. The solid black line is the best fit of our phenomenological model (eq 1). The dashed lines are the repulsion and attraction components of the interexciton potential. $r_0 = 2.6$ nm is the extracted exciton radius. (b) Schematic configuration of a probe exciton (red) among the pump-generated excitons (purple) at different interaction regimes (1−4) as denoted in panel (a).

the effect of exciton−exciton annihilation in the determination of the estimated carrier densities (Supporting Information). This effect has been shown to play a role in highly excited monolayer TMDs.[27,28,31,32] We note that the exponent k differs from the exponent in the Lennard-Jones potential due to the presence of plasma effects in semiconductors, which are not captured by the atomic model. The obtained $r_0 = 2.6$ nm represents the exciton Bohr radius in monolayer WS_2. This value agrees well with our calculated exciton radius (2.3 nm, Supporting Information) and the estimated radius (1−3 nm) in other studies.[11,33,34]

Excitons have been perceived as the solid-state counterpart of atoms, but the analogy is usually drawn only for their similar internal structure and molecular structures. The latter is

apparent from the formation of trions[35−37] and biexcitons[14,15,38−40] with binding energies of 20−60 meV in monolayer TMDs that are analogous to the hydrogen anion and hydrogen molecules. Here, the good agreement between the modified Lennard-Jones model and our experiments reveals further that they also share similar mutual interaction behavior at long and short distances. This finding is remarkable because high-density excitons are usually unstable against the electron−hole plasma formation and other annihilation processes. These competing processes can easily destroy the exciton resonance features and hinder the observation of interexciton repulsion. Monolayer WS_2 is, however, an exceptional material, which hosts tightly bound excitons with radius approaching the atomic limit. The robustness of these excitons helps maintain their resonance features even at very high density. We can therefore observe an effective attraction−repulsion crossover of excitonic interactions, a phenomenon that was predicted early[41] but remained unobserved experimentally until now.

Although the observed shift mimics the Lennard-Jones potential, there are three features distinct from atoms that deserve more careful attention. First, in addition to excitons, plasma can be present simultaneously with a relative density governed by the law of mass action. The interparticle separation r_s is derived from their combined densities. Second, plasma contribution to the shift at low density dominates the exciton contribution. The observed $\sim 1/r_s$ dependence, instead of $1/r_s^6$, indicates a negligible contribution from excitonic van der Waals attraction. This is not surprising because excitons in monolayer TMDs are tightly bound. Third, a possible formation of biexcitons at short distance is not explicitly captured in this model. This is a similar situation faced by Lennard-Jones potential because it does not explicitly represent chemical bonding between atoms, but it can explain why a cluster of atoms can form at the minimum potential. Although biexciton formation may occur at the minimum potential (Figure 3a), the strong plasma screening precludes such occurrence. This is evidenced from the much reduced exciton binding energy at such a high excitation density (Figure 2b). This means biexciton binding energy should also be reduced to a value much smaller than the reported values, or completely screened, and thus unlikely to form.

We can further test our model (eq 1) through its temperature-dependent behavior. Two effects arise when the exciton temperature is high. First, such highly energetic excitons will be in constant motion and dynamically average out their short-range and long-range interactions among each other. Second, the excitons will have higher probability to reach their internal excited states. These effects will reduce the effective potential energy and increase their Bohr radius. As a consequence, the energy potential well between the excitons will become *shallower* and the interexciton distance at the potential minimum will become *wider* (inset of Figure 4c). In other words, when the excitons cool from very high to low temperature, we predict a significant redshift of their energy. As we discuss below, our model captures the complex cooling dynamics and offers a simple interpretation based on such exciton picture, although rigorous contribution from plasma effects could be included for a more accurate model.

This prediction can be conveniently explored in the cooling dynamics of excitons after pump excitation at high density regime, where exciton−exciton interaction dominates, and the exciton picture is particularly appropriate. As we pump monolayer WS_2 using 3.16 eV photons ($h\nu > E_A$), we create
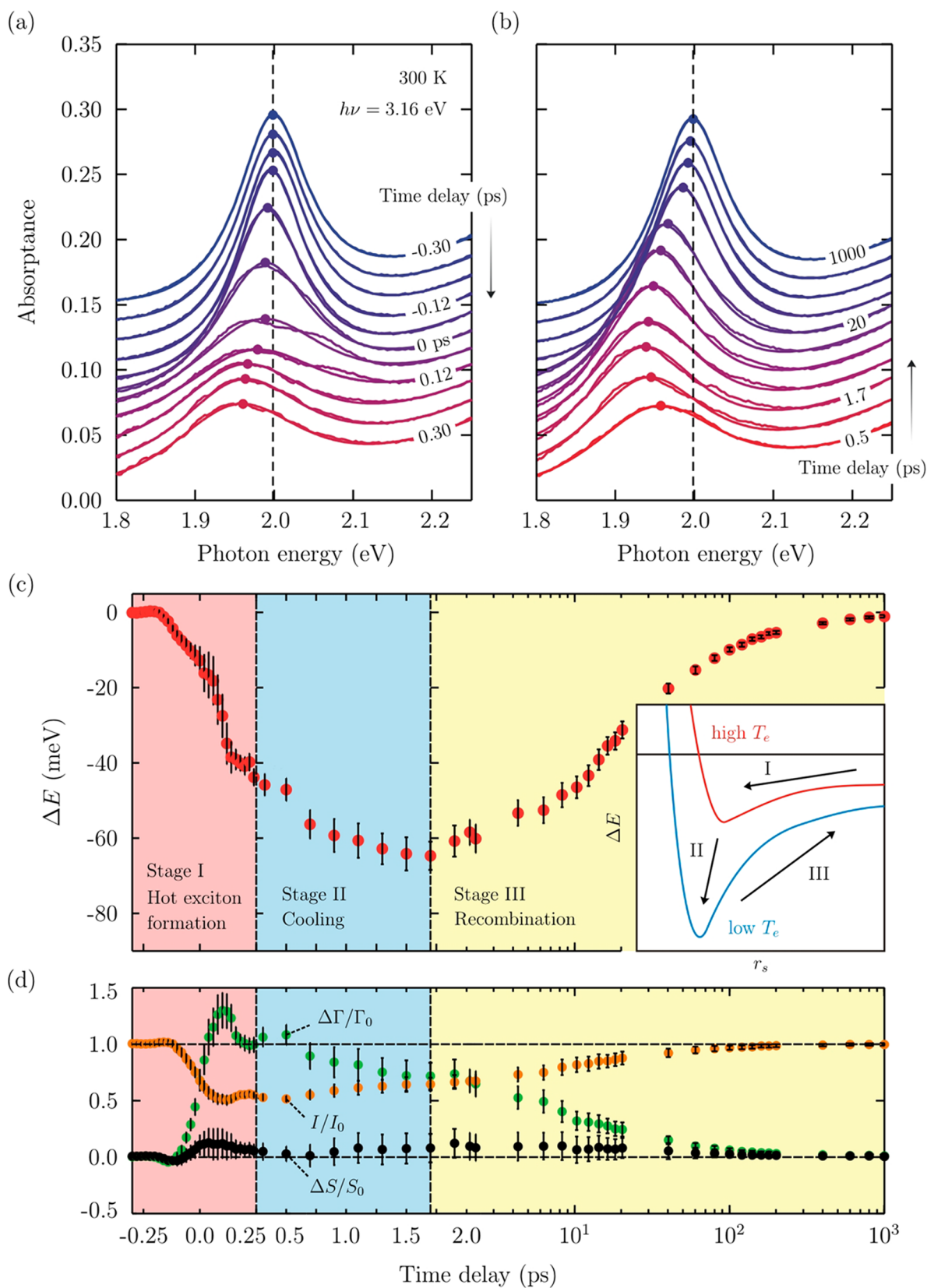
Figure 4. (a,b) Exciton absorption peak at increasing time delays from −0.30 to 0.30 ps (a) and from 0.5 to 1000 ps (b), where only the subset of the data is shown for clarity. The fitting lines (smooth lines) are superimposed with the data curves. (c) Exciton energy shift (ΔE), (d) peak height (I/I_0), line width broadening ($\Delta\Gamma/\Gamma_0$), and spectral weight change ($\Delta S/S_0$). Inset in (c) shows the stages of relaxation dynamics through the ΔE vs r_s curve at high and low temperatures.

free electron−hole pairs that immediately form excitons within the excitation pulse duration.[42,43] This is due to the strong Coulomb attraction in monolayer WS_2 that leads to a very rapid exciton formation. The large excess energy will bring the excitons to a high temperature ($T_e > 1000$ K). Subsequently, we can follow the time evolution of the exciton resonance as they cool down. Figure 4a,b shows a time series of the exciton absorption spectra up to 1 ns ($F = 11 \ \mu J/cm^2$), from which we extract their peak parameters (Figure 4c,d). By examining these parameters, the exciton dynamics can be described roughly in three stages.

In Stage I (red region), the hot excitons are formed with rapidly decreasing interexciton distance, accompanied by a dramatic energy redshift and spectral broadening. In Stage II (blue), the hot excitons cool to the lattice temperature via phonon emission. In Stage III (yellow), the excitons recombine gradually with increasing interexciton distance leading to a blueshift. In the framework of our model, such exciton dynamics can be adequately described by the trajectory (I → II → III) between the hot and cold potential energy curves, as illustrated in the inset of Figure 4c. We exclude possible contribution from lattice cooling in Stage III because the estimated temperature-dependent energy shift is merely ∼4 meV (20 K), far too small than the observed shift ∼70 meV (Supporting Information). It is particularly noteworthy to examine the dynamics in Stage II, where the excitons cool down from $T_e > 1000$ K to ∼300 K, but the density should remain unchanged. As depicted by arrow II in the inset of Figure 4c, the exciton energy decreases when the high-temperature potential curve (red) evolves into the low-temperature curve (blue). During this process, the exciton energy is found to redshift for about 20 meV, accompanied by a decrease of line width. With this interpretation, we can assign to Stage II an exciton cooling time of 2 ps, comparable with the cooling time measured in graphene.[44]

In summary, we have observed a transition of interexcitonic interaction at increasing exciton density in monolayer WS_2, which manifests as a redshift−blueshift crossover of the exciton resonance energy. At low density, the exciton redshift arises from plasma screening effects and the long-range exciton−exciton attraction. At high density, the exciton blueshift is attributed to the short-range exciton−exciton repulsion. We describe this density dependence of the excitonic interactions by a phenomenological model, in analogy to the Lennard-Jones interaction between atoms, combined with a material-realistic computation of plasma effects. Interpreting the time dependence of energy shifts shortly after the carrier excitation in terms of our model, we extract an exciton cooling time of about 2 ps. Similar results are also observed in monolayer MoS_2, implying that this behavior is ubiquitous in monolayer TMD semiconductors.[14] The close analogy between the excitons and atoms, as shown in our experiment, suggests that the liquid and crystal phases of excitons[45−47] can be realized in 2D materials.

ASSOCIATED CONTENT

Ⓢ Supporting Information

The Supporting Information is available free of charge on the ACS Publications website at DOI: 10.1021/acs.nano-lett.7b01034.

Experimental methods; Kramers−Kronig analysis; Maxwell's equations for monolayer materials; fitting analysis; microscopic many-body computation; exciton−exciton annihilation effect; heat capacity and estimated temperature (PDF)

AUTHOR INFORMATION

Corresponding Author

*E-mail: gedik@mit.edu.

ORCID ⊙

J. Kong: 0000-0003-0551-1208

N. Gedik: 0000-0002-6394-4987

Notes

The authors declare no competing financial interest.

REFERENCES

(1) Lennard-Jones, J. E. *Proc. R. Soc. London, Ser. A* **1924**, *106*, 463.

(2) Lennard-Jones, J. E. *Proc. Phys. Soc.* **1931**, *43*, 461.

(3) Mock, J. B.; Thomas, G. A.; Combescot, M. *Solid State Commun.* **1978**, *25*, 279−282.

(4) Semkat, D.; Richter, F.; Kremp, D.; Manzke, G.; Kraeft, W.-D.; Henneberger, K. *Phys. Rev. B: Condens. Matter Mater. Phys.* **2009**, *80*, 155201.

(5) Steinhoff, A.; Rösner, M.; Jahnke, F.; Wehling, T. O.; Gies, C. *Nano Lett.* **2014**, *14*, 3743−3748.

(6) Zimmermann, R. *Phys. Status Solidi B* **2006**, *243*, 2358−2362.

(7) Mak, K. F.; Lee, C.; Hone, J.; Shan, J.; Heinz, T. F. *Phys. Rev. Lett.* **2010**, *105*, 136805.

(8) Ugeda, M. M.; Bradley, A. J.; Shi, S.-F.; da Jornada, F. H.; Zhang, Y.; Qiu, D. Y.; Ruan, W.; Mo, S.-K.; Hussain, Z.; Shen, Z.-X.; Wang, F.; Louie, S. G.; Crommie, M. F. *Nat. Mater.* **2014**, *13*, 1091−1095.

(9) Hill, H. M.; Rigosi, A. F.; Roquelet, C.; Chernikov, A.; Berkelbach, T. C.; Reichman, D. R.; Hybertsen, M. S.; Brus, L. E.; Heinz, T. F. *Nano Lett.* **2015**, *15*, 2992−2997.

(10) Klots, A. R.; Newaz, A. K. M.; Wang, B.; Prasai, D.; Krzyzanowska, H.; Lin, J.; Caudel, D.; Ghimire, N. J.; Yan, J.; Ivanov, B. L.; Velizhanin, K. A.; Burger, A.; Mandrus, D. G.; Tolk, N. H.; Pantelides, S. T.; Bolotin, K. I. *Sci. Rep.* **2015**, *4*, 6608.

(11) Chernikov, A.; Berkelbach, T. C.; Hill, H. M.; Rigosi, A.; Li, Y.; Aslan, O. B.; Reichman, D. R.; Hybertsen, M. S.; Heinz, T. F. *Phys. Rev. Lett.* **2014**, *113*, 076802.

(12) Chernikov, A.; Ruppert, C.; Hill, H. M.; Rigosi, A. F.; Heinz, T. F. *Nat. Photonics* **2015**, *9*, 466−470.

(13) Pogna, E. A. A.; Marsili, M.; De Fazio, D.; Dal Conte, S.; Manzoni, C.; Sangalli, D.; Yoon, D.; Lombardo, A.; Ferrari, A. C.; Marini, A.; Cerullo, G.; Prezzi, D. *ACS Nano* **2015**, *10*, 1182−1188.

(14) Sie, E. J.; Frenzel, A. J.; Lee, Y.-H.; Kong, J.; Gedik, N. *Phys. Rev. B: Condens. Matter Mater. Phys.* **2015**, *92*, 125417.

(15) Mai, C.; Barrette, A.; Yu, Y.; Semenov, Y. G.; Kim, K. W.; Cao, L.; Gundogdu, K. *Nano Lett.* **2014**, *14*, 202−206.

(16) Schmidt, R.; Berghäuser, G.; Schneider, R.; Selig, M.; Tonndorf, P.; Malic, E.; Knorr, A.; Michaelis de Vasconcellos, S.; Bratschitsch, R. *Nano Lett.* **2016**, *16*, 2945−2950.

(17) Ruppert, C.; Chernikov, A.; Hill, H. M.; Rigosi, A. F.; Heinz, T. F. *Nano Lett.* **2017**, *17*, 644.

(18) Wake, D. R.; Yoon, H. W.; Wolfe, J. P.; Morkoç, H. *Phys. Rev. B: Condens. Matter Mater. Phys.* **1992**, *46*, 13452−13460.

(19) Peyghambarian, N.; Gibbs, H. M.; Jewell, J. L.; Antonetti, A.; Migus, A.; Hulin, D.; Mysyrowicz, A. *Phys. Rev. Lett.* **1984**, *53*, 2433−2436.

(20) Hulin, D.; Mysyrowicz, A.; Antonetti, A.; Migus, A.; Masselink, W. T.; Morkoç, H.; Gibbs, H. M.; Peyghambarian, N. *Phys. Rev. B: Condens. Matter Mater. Phys.* **1986**, *33*, 4389−4391.

(21) Schlaad, K.-H.; Weber, Ch.; Cunningham, J.; Hoof, C. V.; Borghs, G.; Weimann, G.; Schlapp, W.; Nickel, H.; Klingshirn, C. *Phys. Rev. B: Condens. Matter Mater. Phys.* **1991**, *43*, 4268−4275.

(22) Schmitt-Rink, S.; Chemla, D.; Miller, D. *Phys. Rev. B: Condens. Matter Mater. Phys.* **1985**, *32*, 6601−6609.

(23) Lee, Y.-H.; Zhang, X.-Q.; Zhang, W.; Chang, M.-T.; Lin, C.-T.; Chang, K.-D.; Yu, Y.-C.; Wang, J. T.-W.; Chang, C.-S.; Li, L.-J.; Lin, T.-W. *Adv. Mater.* **2012**, *24*, 2320−2325.

(24) Lee, Y.-H.; Yu, L.; Wang, H.; Fang, W.; Ling, X.; Shi, Y.; Lin, C.-T.; Huang, J.-K.; Chang, M.-T.; Chang, C.-S.; Dresselhaus, M.; Palacios, T.; Li, L.-J.; Kong, J. *Nano Lett.* **2013**, *13*, 1852−1857.

(25) Gutiérrez, H. R.; Perea-López, N.; Elías, A. L.; Berkdemir, A.; Wang, B.; Lv, R.; López-Urías, F.; Crespi, V. H.; Terrones, H.; Terrones, M. *Nano Lett.* **2013**, *13*, 3447−3454.

(26) Li, Y.; Chernikov, A.; Zhang, X.; Rigosi, A.; Hill, H. M.; van der Zande, A. M.; Chenet, D. A.; Shih, E.-M.; Hone, J.; Heinz, T. F. *Phys. Rev. B: Condens. Matter Mater. Phys.* **2014**, *90*, 205422.

(27) Yu, Y.; Yu, Y.; Xu, C.; Barrette, A.; Gundogdu, K.; Cao, L. *Phys. Rev. B: Condens. Matter Mater. Phys.* **2016**, *93*, 201111.

(28) Sun, D.; Rao, Y.; Reider, G. A.; Chen, G.; You, Y.; Brezin, L.; Harutyunyan, A. R.; Heinz, T. F. *Nano Lett.* **2014**, *14*, 5625−5629.

(29) Chen, Y.; Wen, W.; Zhu, Y.; Mao, N.; Feng, Q.; Zhang, M.; Hsu, H.-P.; Zhang, J.; Huang, Y.-S.; Xie, L. *Nanotechnology* **2016**, *27*, 445705.

(30) Rösner, M.; Şaşıoğlu, E.; Friedrich, C.; Blügel, S.; Wehling, T. O. *Phys. Rev. B: Condens. Matter Mater. Phys.* **2015**, *92*, 085102.

(31) Yuan, L.; Huang, L. *Nanoscale* **2015**, *7*, 7402−7408.

(32) Cunningham, P. D.; McCreary, K. M.; Jonker, B. T. *J. Phys. Chem. Lett.* **2016**, *7*, 5242−5246.

(33) Stier, A. V.; McCreary, K. M.; Jonker, B. T.; Kono, J.; Crooker, S. A. *Nat. Commun.* **2016**, *7*, 10643.

(34) Berkelbach, T. C.; Hybertsen, M. S.; Reichman, D. R. *Phys. Rev. B: Condens. Matter Mater. Phys.* **2013**, *88*, 045318.

(35) Mak, K. F.; He, K.; Lee, C.; Lee, G. H.; Hone, J.; Heinz, T. F.; Shan, J. *Nat. Mater.* **2013**, *12*, 207−211.

(36) Ross, J. S.; Wu, S.; Yu, H.; Ghimire, N. J.; Jones, A. M.; Aivazian, G.; Yan, J.; Mandrus, D. G.; Xiao, D.; Yao, W.; Xu, X. *Nat. Commun.* **2013**, *4*, 1474.

(37) Lui, C. H.; Frenzel, A. J.; Pilon, D. V.; Lee, Y.-H.; Ling, X.; Akselrod, G. M.; Kong, J.; Gedik, N. *Phys. Rev. Lett.* **2014**, *113*, 166801.

(38) Shang, J.; Shen, X.; Cong, C.; Peimyoo, N.; Cao, B.; Eginligil, M.; Yu, T. *ACS Nano* **2015**, *9*, 647−655.

(39) You, Y.; Zhang, X.-X.; Berkelbach, T. C.; Hybertsen, M. S.; Reichman, D. R.; Heinz, T. F. *Nat. Phys.* **2015**, *11*, 477−481.

(40) Hao, K.; Xu, L.; Specht, J. F.; Nagler, P.; Tran, K.; Singh, A.; Dass, C. K.; Schuller, C.; Korn, T.; Richter, M.; Knorr, A.; Li, X.; Moody, G. arXiv: 1609.02008.

(41) Schindler, C.; Zimmermann, R. *Phys. Rev. B: Condens. Matter Mater. Phys.* **2008**, *78*, 045313.

(42) Steinleitner, P.; Merkl, P.; Nagler, P.; Mornhinweg, J.; Schuller, C.; Korn, T.; Chernikov, A.; Huber, R. *Nano Lett.* **2017**, *17*, 1455−1460.

(43) Ceballos, F.; Cui, Q.; Bellus, M. Z.; Zhao, H. *Nanoscale* **2016**, *8*, 11681−11688.

(44) Gao, B.; Hartland, G.; Fang, T.; Kelly, M.; Jena, D.; Xing, H.; Huang, L. *Nano Lett.* **2011**, *11*, 3184−3189.

(45) Handel, P. H.; Kittel, C. *Proc. Natl. Acad. Sci. U. S. A.* **1971**, *68*, 3120−3121.

(46) Ivanov, A. L.; Haug, H. *Phys. Rev. Lett.* **1993**, *71*, 3182−3185.

(47) Böning, J.; Filinov, A.; Bonitz, M. *Phys. Rev. B: Condens. Matter Mater. Phys.* **2011**, *84*, 075130.